Journal Pre-proofs

Production of negative-emission biomethane by twin double-bed pressure swing adsorption with tail gas sequestration

Ayub Golmakani, Seyed Ali Nabavi, Vasilije Manović

PII: S1385-8947(20)33436-7
DOI: https://doi.org/10.1016/j.cej.2020.127312
Reference: CEJ 127312

To appear in: *Chemical Engineering Journal*

Received Date: 27 May 2020
Revised Date: 6 October 2020
Accepted Date: 7 October 2020

Please cite this article as: A. Golmakani, S. Ali Nabavi, V. Manović, Production of negative-emission biomethane by twin double-bed pressure swing adsorption with tail gas sequestration, *Chemical Engineering Journal* (2020), doi: https://doi.org/10.1016/j.cej.2020.127312

Chemical Engineering Journal, Volume 408, March 2021, Article number 127312
DOI:10.1016/j.cej.2020.127312

Production of negative-emission biomethane by twin double-bed pressure swing adsorption with tail gas sequestration

Ayub Golmakani, Seyed Ali Nabavi, Vasilije Manović*

Centre for Climate and Environmental Protection, Cranfield University, Bedford, Bedfordshire MK43 0AL, UK

*Corresponding author: Vasilije Manović (v.manovic@cranfield.ac.uk)

Abstract

Selective removal of CO_2 during biogas upgrading and subsequent sequestration can transform the produced biomethane from a carbon-neutral to carbon-negative energy source. Such technology can be considered as bioenergy with carbon capture and storage (BECCS), i.e., as a negative-emission technology (NET). In this research, porous polymeric beads (PPBs) with a practical working capacity above atmospheric pressure and cyclic performance were developed to be used for biogas upgrading by pressure swing adsorption (PSA) without the need for vacuum. The CO_2 and CH_4 equilibrium isotherms of PPBs were measured in the temperature range of 0-70 °C and in the pressure range of 0-10 bar. The dynamic breakthrough curves of 40:60 (vol%) CO_2/CH_4 gas mixture were measured at 2 bar and 10 bar. These isotherms and breakthrough curves were used as inputs in a dynamic PSA simulation model to predict the performance of a twin double-bed PSA biogas upgrading process. The model indicated that biomethane with 91% CH_4 recovery can be produced and a stream of >90% CO_2 purity from the tail gas, suitable for geological storage, can be separated. It should be highlighted that unlike

current state-of-the-art PSA units, the proposed process using PPBs can upgrade biogas with minimal energy consumption for regeneration of adsorbents. The proposed selective tail gas separation scheme can be used to produce carbon-negative biomethane.

Keywords: biogas upgrading; pressure swing adsorption; PSA; biomethane; carbon sequestration; negative-emission technologies

1 Introduction

Due to anthropogenic greenhouse gas emissions (GHG) and the urgency to mitigate global warming, the Intergovernmental Panel on Climate Change (IPCC) in 2019 recommended to limit the average global warming to 1.5 °C[1]. To achieve this target, it is required to reduce CO_2 emissions by 50% by 2030 compared to 1990 levels and to achieve net-zero emissions by 2050, which requires deployment of negative-emission technologies (NET)[2,3]. Carbon-negative fuels are expected to play a key role in NET roll-out[4]. Biogas, which is predominantly a mixture of CO_2/CH_4 produced from natural feedstocks such as agricultural and food wastes, can be considered as a carbon-neutral fuel[5–8]. Moreover, biogas upgrading and separating CO_2 of high purity, with specifications required for sequestration, converts the produced biomethane from a carbon-neutral to carbon-negative fuel[9–11].

Adsorption technologies have been a promising route for biogas upgrading, and have been commercially deployed due to their low energy demand, low capital investment and operational costs[12–14]. Their continuous operation is achieved by three main types of cyclic adsorption processes: pressure swing adsorption (PSA), pressure vacuum swing adsorption (PVSA), and temperature swing adsorption (TSA)[15–18]. PVSA and TSA units require vacuum and heat for adsorbent regeneration, respectively, while PSA does not require energy for this step[19]. Most state-of-the-art cyclic adsorption processes used for biogas upgrading are based on PVSA[12,20,21]. Several process parameters and components affect the PVSA performance, including the number of beds, operating pressure, number of cycle steps, step duration, vacuum level, and the adsorbent type[12,20–22].

The adsorbents are the most critical components of the adsorption processes and can be classified into three categories: equilibrium, kinetic and functionalised. The equilibrium-based adsorbents, such as activated carbons and zeolite 13X, are characterised by higher adsorption capacity of CO_2 when compared to that of CH_4[23]. The kinetic adsorbents, such as carbon molecular sieves, clinoptilolites, titanosilicates, and some metal organic frameworks (MOFs), operate based on the difference in the rate of CO_2 and CH_4 uptake. The size of their micropores is designed to be in the range where more CO_2 is retained per unit of time[20]. The functionalised adsorbents are a new class of materials recently used for biogas upgrading. Mafra et al.[22] investigated SBA-15 functionalised by different amine groups. They found that the CO_2/CH_4 selectivity of primary, secondary, tertiary and mixed primary/secondary amine-functionalised adsorbents was 40, 1000, 6 and 11000, respectively. Although primary amines had lower selectivity when compared to secondary and mixed amine-functionalised adsorbents, they were proposed for biogas upgrading due to their linear adsorption isotherms that make their regeneration easier. The amine-functionalised adsorbents have higher CO_2/CH_4 selectivity when compared to traditional adsorbents, but they suffer from low chemical stability. Their adsorption capacity decreases after each adsorption/regeneration cycle, which is a challenge for their industrial deployment[24]. Another disadvantage is low adsorption rate. An ideal adsorbent for biogas upgrading is featured with high CO_2/CH_4 selectivity, high CO_2 capacity, cyclic stability and ease of regeneration.

The performance of adsorbents must be evaluated by means of CH_4 purity, recovery, energy consumption, and CO_2 purity in the tail gas after several cycles in PVSA units. Canevesi et al.[12] produced biomethane with 97.5% CH_4 purity and 93.5% CH_4 recovery in a two-bed PSA unit. They used carbon molecular sieves as a kinetic-based adsorbent, which required high energy

consumption for adsorbent regeneration during the vacuum (VA) and purge (PG) steps for bed evacuation up to 0.1 bar. Grande et al.[25] used zeolite 13X as an equilibrium-based adsorbent in a PSA unit and produced biomethane with 98% purity and 60% CH_4 recovery, with adsorbent regeneration under vacuum. Moreover, they demonstrated that CH_4 recovery can be increased up to 80% with a layered configuration of carbon molecular sieves/13X[25]. The required electricity consumption during the PG step for maintaining vacuum level of 0.1 bar in the bed was as high as 2125 kJ/kg CH_4[25]. Wu et al.[26] reported that the electrical energy demand required for the operation of a PVSA unit loaded by MOF, Zeolite 13x, and CMS-3K is 944, 2155, and 1093 kJ/kg CH_4, respectively. Augelletti et al.[21] used Zeolite 5A as an equilibrium-based adsorbent for biogas upgrading in two PVSA units. They obtained a CH_4 recovery of 99% with energy consumption of 1250 kJ/kg CH_4. The high energy consumption was related to the nonlinear isotherm behaviour of Zeolite 5A that required extreme vacuum for adsorbent regeneration.

Therefore, it can be noted that in state-of-the-art PSA units for biogas upgrading, either energy consumption is high or CH_4 recovery is low, i.e., the units with high CH_4 recovery require high electrical energy consumption for bed regeneration. Moreover, although the adsorption processes are usually regarded as PSA, in fact, they are PVSA. Developing PSA processes that do not require vacuum, i.e., the adsorbent regeneration is performed at atmospheric pressure, would enhance and promote adsorption technologies as a viable choice for biogas upgrading.

In this study, a novel porous polymeric bead (PPB) adsorbent with linear adsorption isotherms and acceptable working capacity above atmospheric pressure is developed and its cyclic performance in PSA processes is explored. This adsorbent was developed to operate in PSA units without vacuum requirement for the regeneration step. The equilibrium adsorption

isotherms and breakthrough curves of CO_2 and CH_4 for the PPB adsorbent were measured at different temperatures and pressures. In order to simulate the performance of the PSA process for biogas upgrading, a dynamic PSA simulation model was developed, which incorporates the isotherm parameters and mass transfer coefficients (MTCs) obtained by fitting the model predictions and the breakthrough curves. A twin double-bed PSA unit for biogas upgrading was proposed and simulated. Finally, selective tail gas sequestration was proposed, which enables biogas production and upgrading to be a NET rather than carbon-neutral technology.

2 Process description

The proposed biogas upgrading process consists of two PSA units, as presented in Figure 1. The first two-bed PSA unit upgrades biogas to biomethane with high purity, but moderate recovery. The tail gas of this unit is then processed in the second two-bed PSA unit to further increase the overall recovery and CO_2 purity in the tail gas. The tail gas of the first PSA unit, which is composed of blow down (BD) and purge (PG) streams of CO_2 (low purity) is not suitable for storage; therefore, the second two-bed PSA unit situated downstream is used to enhance both CO_2 purity and CH_4 recovery. Moreover, during the periods of high CO_2 purity in the tail gas downstream of the process, concentrated CO_2 stream is proposed to be either compressed for underground storage or utilised, while the tail gas stream, during the periods of relatively higher CH_4 concentration, is utilised in processes such as combined heat and power (CHP), as illustrated in Figure 1. This approach can be considered as a type of bioenergy with carbon capture and storage (BECCS), i.e., as a negative-CO_2-emission process.

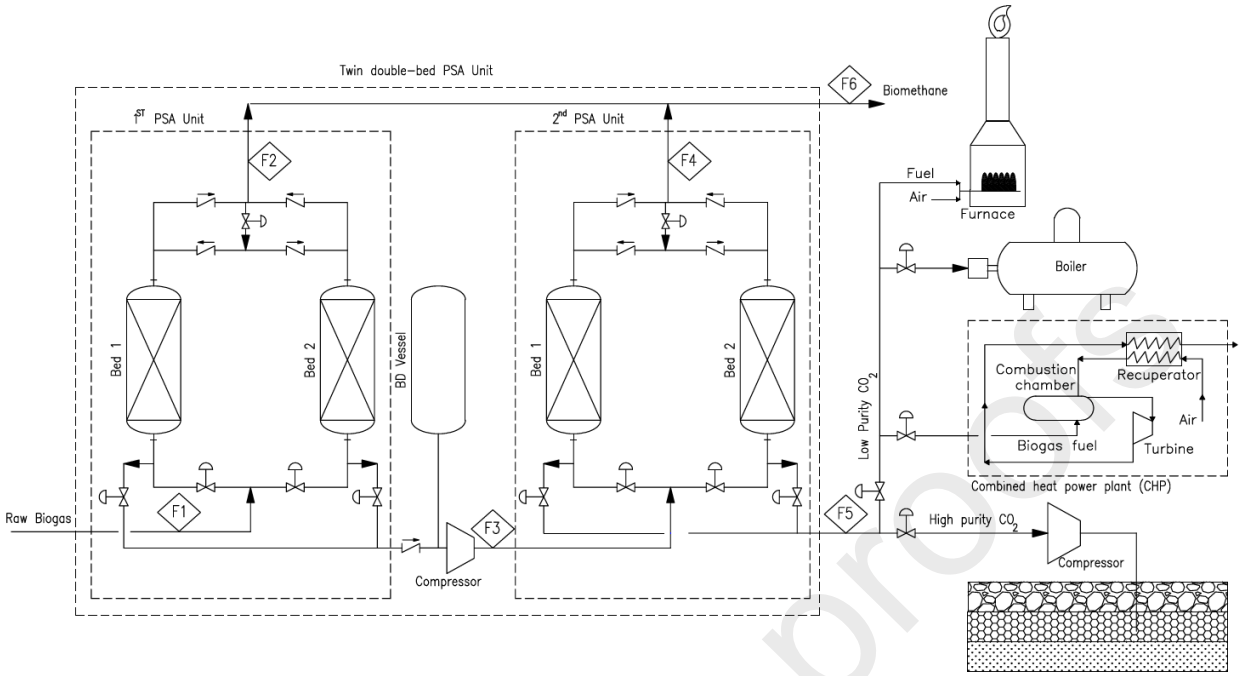

Figure 1: Schematics of twin double-bed PSA concept for biogas upgrading with selective tail gas sequestration. F1: feed molar flowrate to 1st PSA, F2: effluent product molar flowrate from 1st PSA, F3: feed molar flowrate to 2nd PSA, F4: effluent product molar flowrate from 2nd PSA, F5: effluent tail gas molar flowrate from 2nd PSA. F6: effluent product molar flowrate from twin double-bed PSA unit.

The bed conditions and step durations of the proposed PSA process are depicted in Figure 2. It can be seen that every cycle comprises six steps, including one equalisation step for enhancing CH_4 recovery. A portion of the biomethane product from the bed at the adsorption (AD) step is used for regeneration of the bed that is at the PG step. It should be noted that, unlike state-of-the-art PSA processes for biogas upgrading[25,26], no vacuum is needed to regenerate the adsorbent during purge (PG) steps.

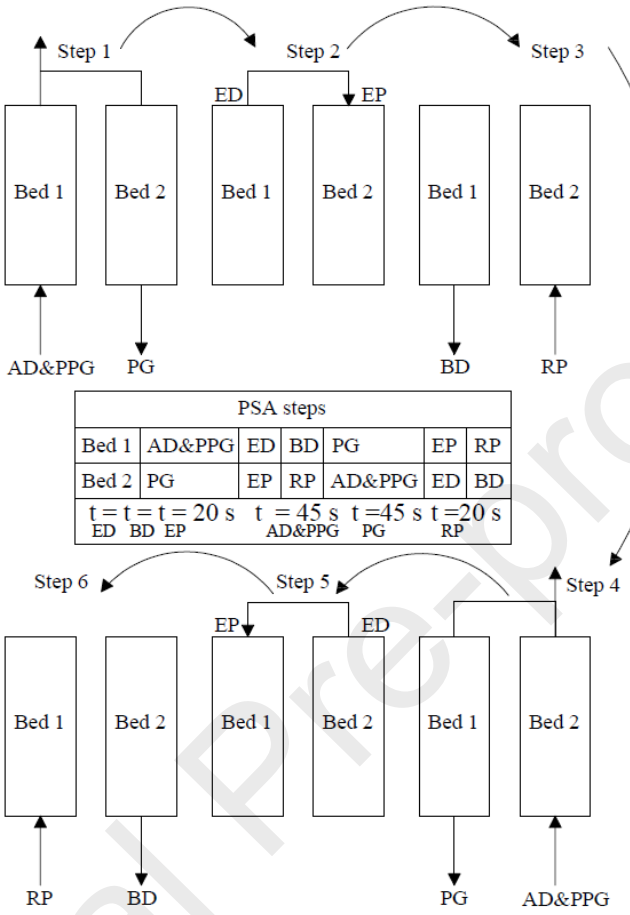

Figure 2: Schematic representation of the steps for each PSA unit of the proposed biogas upgrading process. AD: adsorption, BD: blow down, ED: equalisation depressurisation, EP: equalisation pressurisation, PPG: providing purge, PG: purge, and RP: repressurisation.

3 Mathematical model

The steps for both cyclic adsorption units of the PSA process were simulated using one dynamic PSA simulation model. It was assumed that considered gases (CO_2 and CH_4) follow the ideal gas law. The bed and particle porosity were assumed to be uniform along the bed, and the radial

gradients of gas concentrations and temperature were neglected. The heat transfer for gas, adsorbent and bed walls were considered. The dispersed plug flow was assumed, and the pressure drop over the bed was estimated by the Ergun equation. The linear driving force (LDF) model was used for the lumped resistance model, and the dual-site Langmuir model was used for the prediction of equilibrium loadings.

The partial differential equations (PDEs) for the mass balance, momentum, and heat balance for gas, adsorbent and wall are presented in Table 1. These PDEs were discretised by the finite difference method, and the obtained ordinary differential equations (ODEs) were solved by the implicit Euler method using Aspen Adsorption®. The bed was divided into 40 segments and 1 s time interval was used in solving the ODEs. It was assumed that cyclic steady-state conditions were achieved when the relative tolerance of mole fraction for every product component at the bed outlet in every moment is less than 10^{-6} for two successive cycles (convergence criterion).

Table 1. Partial differential equations (PDEs) of the dynamic PSA simulation model[a].

Description	**Formulation**	
Mass balance for component *i* in gas phase	$\frac{\partial}{\partial z}\left(\varepsilon D_z c_{gT} \frac{\partial y_i}{\partial z}\right) - \frac{\partial}{\partial z}\left(u_s c_{g,i}\right) - \varepsilon \frac{\partial c_{g,i}}{\partial t} - (1-\varepsilon)\rho_p \frac{\partial q_i}{\partial t} = 0$	(1)
Gas-to-particle mass transfer (LDF model)	$\frac{\partial q_i}{\partial t} = MTC_i(q_i^* - q_i)$	(2)
Dual-site Langmuir model for equilibrium adsorption isotherms	$q_i^* = \frac{k_{1,i}\, e^{\frac{k_{2,i}}{T}} P_i}{1 + \sum_i \; k_{3,i}\, e^{\frac{k_{4,i}}{T}} P_i} + \frac{k_{5,i}\, e^{\frac{k_{6,i}}{T}} P_i}{1 + \sum_i \; k_{7,i}\, e^{\frac{k_{8,i}}{T}} P_i}$	(3)

Heat balance for gas bulk

$$\frac{\partial}{\partial z}\left(\lambda\frac{\partial T_g}{\partial z}\right) - c_{gT}C_p\frac{\partial(u_s T_g)}{\partial z} - \varepsilon C_v T_g\frac{\partial c_{gT}}{\partial t} - (1-\varepsilon)a_p h_f\left(T_g - T_p\right) - \frac{4h_w}{2r_{bi}}\left(T_g - T_w\right) - \varepsilon c_{gT}C_v\frac{\partial T_g}{\partial t} = 0 \quad (4)$$

Heat balance for adsorbent

$$(1-\varepsilon)\left[\rho_p\sum_{i=1}^{n}q_i C_{v,ads,i} + \rho_p C_{ps}\right]\frac{\partial T_p}{\partial t} = \rho_b\sum_{i=1}^{n}(-\Delta H_{ads})_i\frac{\partial q_i}{\partial t} \quad (5)$$

Heat balance for bed wall

$$\rho_w C_{pw} A_w\frac{\partial T_w}{\partial t} = 2\pi r_{bi}h_w\left(T_g - T_w\right) - 2\pi r_{bo}h_o(T_w - T_{atm}) \quad (6)$$

Effective axial heat dispersion coefficient[27,28]

$$\frac{\lambda}{k_g} = 7 + 0.5\,Re\,Pr \quad (7)$$

Heat transfer coefficient between particle and gas[27,29]

$$Nu_f = \frac{h_f d_p}{k_g} = 2 + 1.1\,Pr^{1/3}Re^{0.6} \quad (8)$$

Heat transfer coefficient between inner wall and gas[30–33]

$$Nu_w = \frac{h_w 2r_{bi}}{k_g} = 12.5 + 0.048\,Re \quad (9)$$

Heat transfer coefficient between outer wall and ambient[34,35]

$$Nu_o = \frac{h_o 2r_{bo}}{k_a} = 0.1\,Ra^{1/3} \quad (10)$$

Ergun equation for momentum balance[36,37]

$$-\frac{\partial P}{\partial z} = \frac{150\,\mu\,(1-\varepsilon)^2}{d_p^2\,\varepsilon^3}u_s + \frac{1.75\;(1-\varepsilon)\;\rho}{d_p\;\varepsilon^3}u_s|u_s| \quad (11)$$

[a] Initial conditions (t = 0) are: $y_{CO2} = 0;\ c_{g,CO2} = 0;\ q_{CO2} = 0;\ y_{CH4} = 1;\ T_g = T_p = T_w = T_{inlet}$

The CH_4 purity in the produced biomethane and CO_2 purity in the tail gas of every single PSA unit were calculated after reaching cyclic steady state conditions using Eqs. (12) and (13):

$$\text{CH}_4 \text{ Purity (\%)} = \frac{\int_O^{t_{ads}} c_{CH_4P} u_{sp}\, dt}{\sum_{i=1}^{n} \int_O^{t_{ads}} c_{ip} u_{sp} dt} \times 100 \quad (12)$$

$$\text{CO}_2 \text{ Purity (\%)} = \frac{\left(\int_O^{t_{BD}} c_{CO_2 t} u_{st} + \int_O^{t_{PG}} c_{CO_2 t} u_{st}\right) dt}{\sum_{i=1}^{n} \left(\int_O^{t_{BD}} c_{it} u_{st} + \int_O^{t_{PG}} c_{it} u_{st}\right) dt} \times 100 \quad (13)$$

The c_{CH_4P} and c_{ip} are methane and component *i* concentrations in product stream, respectively. The terms u_{sp} and u_{st} are superficial velocity at product and tail gas end, respectively. The terms $c_{CO_2 t}$ and c_{it} are concentrations of CO_2 and component *i* at tail gas end, respectively.

The combined CH_4 purity of the twin double-bed PSA unit can be calculated by either Eq.(14) or (15):

$$CH_4\ Purity(\%) = \frac{R_{PSA1} \times Purity_{PSA1} + (1 - R_{PSA1}) \times R_{PSA2} \times Purity_{PSA2}}{R_{PSA1} + (1 - R_{PSA1}) \times R_{PSA2}} \times 100 \quad (14)$$

$$CH_4\ Purity\ (\%) = \frac{F_{2,CH4} + F_{4,CH4}}{F_2 + F_4} \times 100 \quad (15)$$

The F_2 and F_4 are effluent product molar flowrate from 1st and 2nd PSA units, respectively (Figure 1). The $F_{2,CH4}$ and $F_{4,CH4}$ are CH_4 molar flowrates of streams F_2 and F_4, respectively. R_{PSA1} and $Purity_{PSA1}$, and R_{PSA2} and $Purity_{PSA2}$ are recovery and purity of 1st and 2nd PSA units, respectively.

Recovery is the portion of CH_4 in biogas which is converted to biomethane, calculated by Eq. (16) for every single PSA unit:

$$\text{Recovery} = \frac{\int_O^{t_{ads}} c_{CH_4P} u_{sp}\, dt - \int_O^{t_{PG}} c_{CH_4P} u_{sPG}\, dt}{\int_O^{t_{ads}} c_{CH_4f} u_{sf}\, dt + \int_O^{t_{RP}} c_{CH_4f} u_{sf}\, dt} \quad (16)$$

The $c_{CH_4 f}$ is methane concentration at feed while u_{sf} and u_{sPG} are superficial velocity at feed and purge steps, respectively.

The combined CH_4 recovery of twin double-bed PSA unit is calculated by either Eq. (17) or (18):

$$\mathrm{CH_4}\ Recovery(\%) = [R_{PSA1} + (1 - R_{PSA1}) \times R_{PSA2}] \times 100 \quad (17)$$

$$\mathrm{CH_4\ Recovery\ (\%)} = \frac{\mathrm{F_{2,CH4}} + \mathrm{F_{4,CH4}}}{\mathrm{F_{1,CH4}}} \times 100 \quad (18)$$

The $F_{1,CH4}$ is the total CH_4 molar flow rate to the twin double-bed PSA unit during AD and RP steps.

The power consumption of compressors for pressurisation of feed at first and second PSA units is calculated using Eq.(19)[38]:

$$Power\ (W) = F.M\left(\frac{n}{n-1}\right) CF \left(\frac{P_1}{\rho_1}\right)\left[\left(\frac{P_2}{P_1}\right)^{\frac{n-1}{n}} - 1\right] \quad (19)$$

where F is molar flowrate, M is molecular weight, P_1 and P_2 are the pressure of inlet and discharged streams, respectively, and ρ_1 is the density of inlet stream. n and CF are isentropic power factor and correlation factor, respectively, and calculated using Eqs. (20) and (21)[38]:

$$n = \ln\left(\frac{P_2}{P_1}\right) \Big/ \ln\left(\frac{\rho_2'}{\rho_1}\right) \quad (20)$$

$$\mathrm{CF} = \frac{h_2' - h_1}{\left(\frac{\mathrm{n}}{n-1}\right)\left(\frac{P_2}{\rho_2'} - \frac{P_1}{\rho_1}\right)} \tag{21}$$

where ρ_2' and h_2' are density and enthalpy of exit stream, respectively, corresponding to the entropy of the inlet stream.

The static selectivity is calculated based on ideal adsorption solution theory (IAST) using Eq. (22)[39]:

$$S = \frac{q^*_{CO_2}/q^*_{CH_4}}{P_{CO_2}/P_{CH_4}} \tag{22}$$

where $\mathrm{q}^*_{CO_2}$ and $\mathrm{q}^*_{CH_4}$ are equilibrium adsorption capacity of CO_2 and CH_4 at given CO_2 (P_{CO_2}) and CH_4 partial pressure (P_{CH_4}), respectively. The dynamic selectivity of binary mixture of CO_2/CH_4 is calculated using Eq. (23)[40]:

$$S_d = \frac{\mathrm{q}_{CO_2}/q_{CH_4}}{\mathrm{y}_{CO_2}/y_{CH_4}} \tag{23}$$

where q represents loading measured from dynamic breakthrough, and at specific mole fraction (y) in gas phase.

The dynamic adsorption capacity is calculated from the measured breakthrough curves using Eqs. (24) and (25)[41]:

$$q_t = \frac{Q_t C_{0,i} t_q}{m} \tag{24}$$

$$\mathrm{t}_q = \int_0^{\infty} \left(1 - \frac{C_{g,i}}{C_{0,i}}\right) dt \tag{25}$$

Where $c_{0,i}$ and $c_{g,i}$ are concentrations of each component at inlet and outlet of the column. Q_t is the feed volumetric flow rate and m is the adsorbent mass.

4 Experimental section

4.1 Adsorbent synthesis

The poly(AA-co-EGDMA) porous polymeric beads (PPB) were synthesised using the oil-in-oil suspension polymerisation method. The dispersed phase was prepared by dissolving 48 mmol acrylamide (AA), 7.2 mmol 2,2'-azobis(2-methylpropionitrile) (AIBN) and 120 mmol ethyleneglycol dimethacrylate (EGDMA) in 60 mL acetonitrile (AN). The continuous phase was light mineral oil. For suspension polymerisation, 360 mL mineral oil was poured into a 1 L jacketed reactor equipped with a five-neck lid and heated up to 60 °C, using a refrigerated/heating circulator (Julabo, Germany), while agitating with a four-bladed impeller. Then, the dispersed phase was poured into the reactor and the emulsion was purged with nitrogen for 10 minutes, followed by nitrogen blanketing throughout the entire polymerisation for 3 hours. Upon completion of the polymerisation, the PPBs were separated from the mixture (mineral oil and remaining AN), and washed several times with isopropanol, until no traces of any other compound in the solvent were detected using a Beckman Coulter UV-Vis spectrophotometer. PPBs were then filtered and dried overnight at 80 °C.

4.2 Materials characterisation

The BET pore surface area and pore volume of the PPB adsorbent were measured by nitrogen adsorption/desorption at 77 K using a 3P meso apparatus. The BET surface area was obtained from adsorbed nitrogen in relative pressure (P/P_0) range of 0.06-0.30, while the total pore volume was measured at P/P_0 = 0.99. The specific heat capacity was measured using a Universal V4.5A TA Instruments differential scanning calorimeter (DSC). The properties of the synthesised material used for simulations in the dynamic PSA simulation model are provided in Table 2.

Table 2: Adsorbent specifications as model parameters

Parameter	Unit	Value
Particle porosity, ε_p	-	0.322
Pore specific surface area, a_p	m^2/m^3	1479
Particle density, ρ_p	kg/m^3	880
Bulk density, ρ_b	kg/m^3	460
Bulk porosity, ε	-	0.477
Particle radius, r_p	mm	0.5
Specific heat capacity, C_{ps}	kJ/kg·K	1.2

The equilibrium isotherms (static tests) were measured by a mixSorb L instrument in the pressure range of 0-10 bar and the temperature range of 0-70 °C, and breakthrough curves (dynamic tests) were obtained using the experimental setup presented in Figure 3. Both static and dynamic tests were carried out in the 3P INSTRUMENTS GmbH laboratory (Germany). The gas flow rates and gas composition at the inlet of the dynamic setup were controlled by three mass flow controllers (MFC) downstream of CO_2, CH_4 and He cylinders. The concentrations of CO_2

and CH_4 at the bed outlet were measured by an internal thermal conductivity detector (TCD). In order to satisfy the minimum flow rate required for the TCD analyser, helium as an inert gas was injected to increase the flow rate at the bed outlet. The pressure of the adsorption vessel is controlled by a back-pressure regulator (BPR). The dynamic experiments at low pressure (2 bar) and high pressure (10 bar) were performed at two temperatures (0 °C and 25 °C) in order to obtain breakthrough curves, with test conditions specified in Table 3. The gas inlet temperature was controlled by a heat exchanger with water as heat exchange media. The internal diameter of the adsorption cell was 3.0 cm and adsorbent mass was 42.9 g. Before each dynamic test, the sample was regenerated by simultaneous heating and purging with helium under vacuum conditions for three hours.

Table 3: The dynamic test conditions

Parameter	**Unit**	**Low pressure**	**High pressure**
Bed pressure	bar	2	10
Simulated biogas composition	mol%	20% CO_2, 30% CH_4, 50% He	24% CO_2, 36% CH_4, 40% He
Biogas inlet temperature	°C	0, 25	0, 25
Biogas flow rate	mL/min	1000	1320

Note 1: All measurements are taken at standard conditions, 0°C and 1 atm

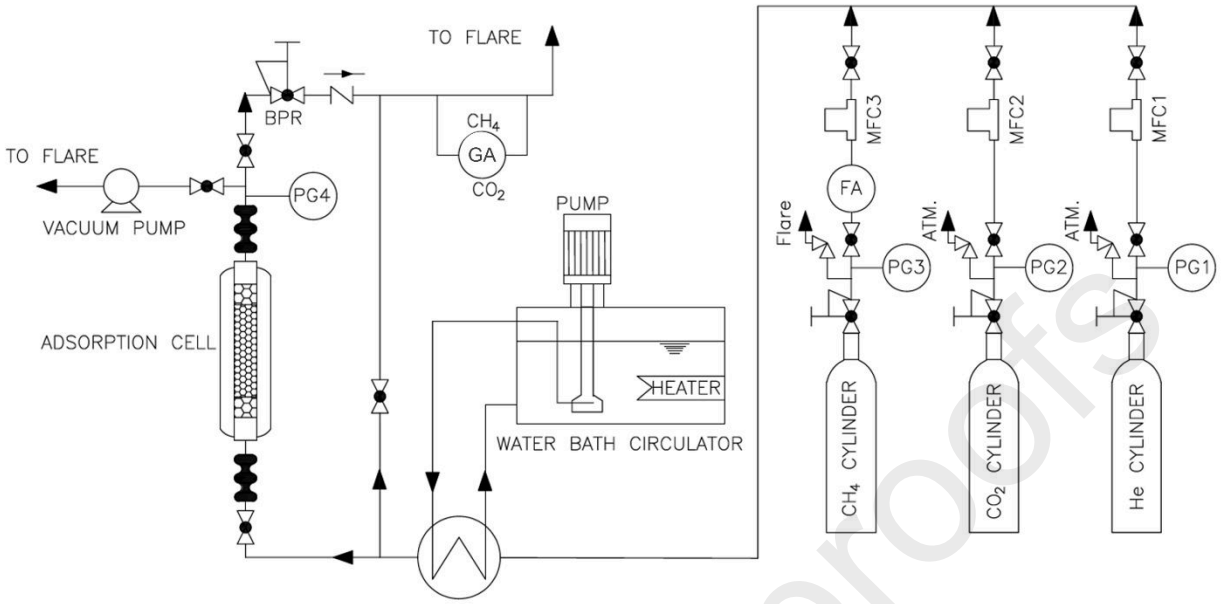

Figure 3: Schematics of dynamic rig for measuring breakthrough curves. ATM: atmosphere, BPR: back-pressure regulator, FA: flame arrestor, MFC: mass flow controller, PG: pressure gauge, and GA: gas analyser.

5 Results and discussion

5.1 Isotherm model and parameters

Figure 4 presents the equilibrium adsorption isotherms of CH_4 and CO_2 for PPB at different temperatures and under pressure in the range of 0-10 bar. The dual-site Langmuir model, Eq. (3), was used to fit the experimental data, and very good agreement was achieved. The model parameters ($k_{j,i}$), and heat of adsorption, were calculated using the least square regression, and are presented in Table 4. It can be seen in Figure 4 that the CO_2 isotherms of PPBs follow a linear pattern in the pressure range of 1-10 bar, which enables PSA operation in this pressure range without the requirement of vacuum for the regeneration step. Also, the linear pattern shows that the adsorbent is characterised by a practical working capacity at pressures above 1 bar,

which enables the design of PSA process systems entirely above atmospheric pressure. Figure 5 presents a comparison of the measured CO_2 isotherm and working capacity (W) of commercial adsorbents with PPB, in a PSA process with 40:60 (vol%) CO_2/CH_4 gas mixture. The total pressure of PG step is 1 bar (CO_2 partial pressure = 0.4 bar), while the total pressure of AD step is 6 bar (CO_2 partial pressure = 2.4 bar). The CO_2 working capacity is defined as the difference in adsorption capacity of CO_2 at PG and AD steps. It can be seen that the CO_2 isotherms of presented commercial sorbents (Zeolite 13x[42], PEI-loaded mesoporous silica[43], and ZSM5[44]) between 0.4 – 2.4 bar CO_2 partial pressure is featured with a gradual slope in comparison with PPB. This indicates that the working capacity of PPB is superior, even though the CO_2 capture capacities of some of those sorbents are larger in this range. To utilise those commercial sorbents for biogas upgrading, extreme vacuum is needed to achieve a practical working capacity[2,12,20], which can lead to significant energy demand.

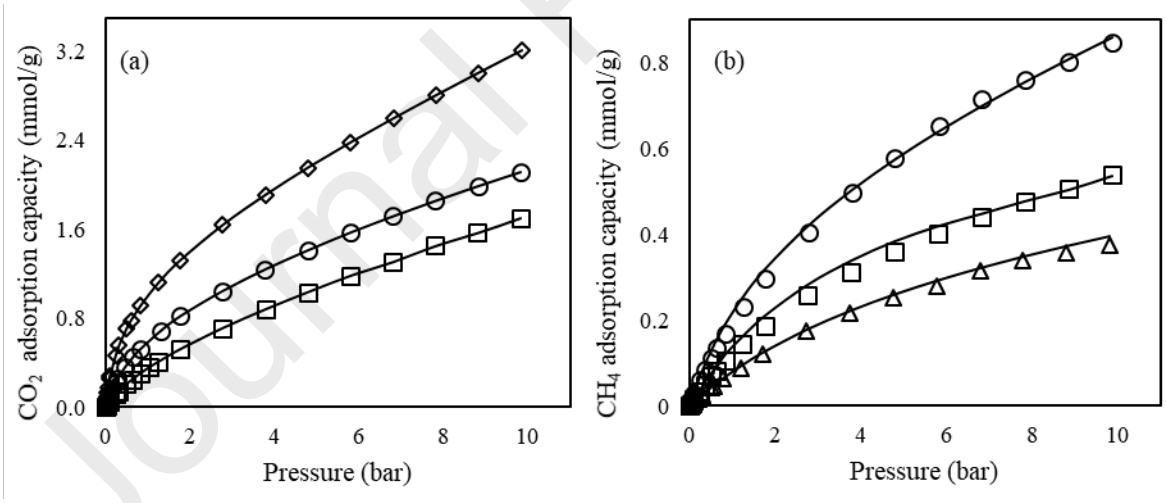

Figure 4: Results of static experiments with PPB adsorbents fitted by the dual-site Langmuir model: (a) CO_2 and (b) CH_4. Legend: Solid lines are dual-site Langmuir model fitting curves, and symbols are experimental results (◊ 0 °C, ○ 25 °C, □ 50 °C, and Δ 70 °C).

Table 4: Dual-site Langmuir model parameters for fitting CO_2 and CH_4 isotherms of PPB adsorbent

Parameter	Unit	CO_2	CH_4
$k_{1,i}$	kmol/(kg·bar)	4.55×10^{-8}	6.31×10^{-10}
$k_{2,i}$	K	2415.74	3415.67
$k_{3,i}$	1/bar	4.37×10^{-6}	1.82×10^{-7}
$k_{4,i}$	K	2415.74	3415.67
$k_{5,i}$	kmol/(kg·bar)	1.62×10^{-7}	2.83×10^{-8}
$k_{6,i}$	K	2587.52	2718.98
$k_{7,i}$	1/bar	1.75×10^{-4}	6.83×10^{-5}
$k_{8,i}$	K	2587.52	2718.98
R^2	(-)	0.99991	0.99978
ΔH_{ads}	kJ/mol	-17.77	-15.66

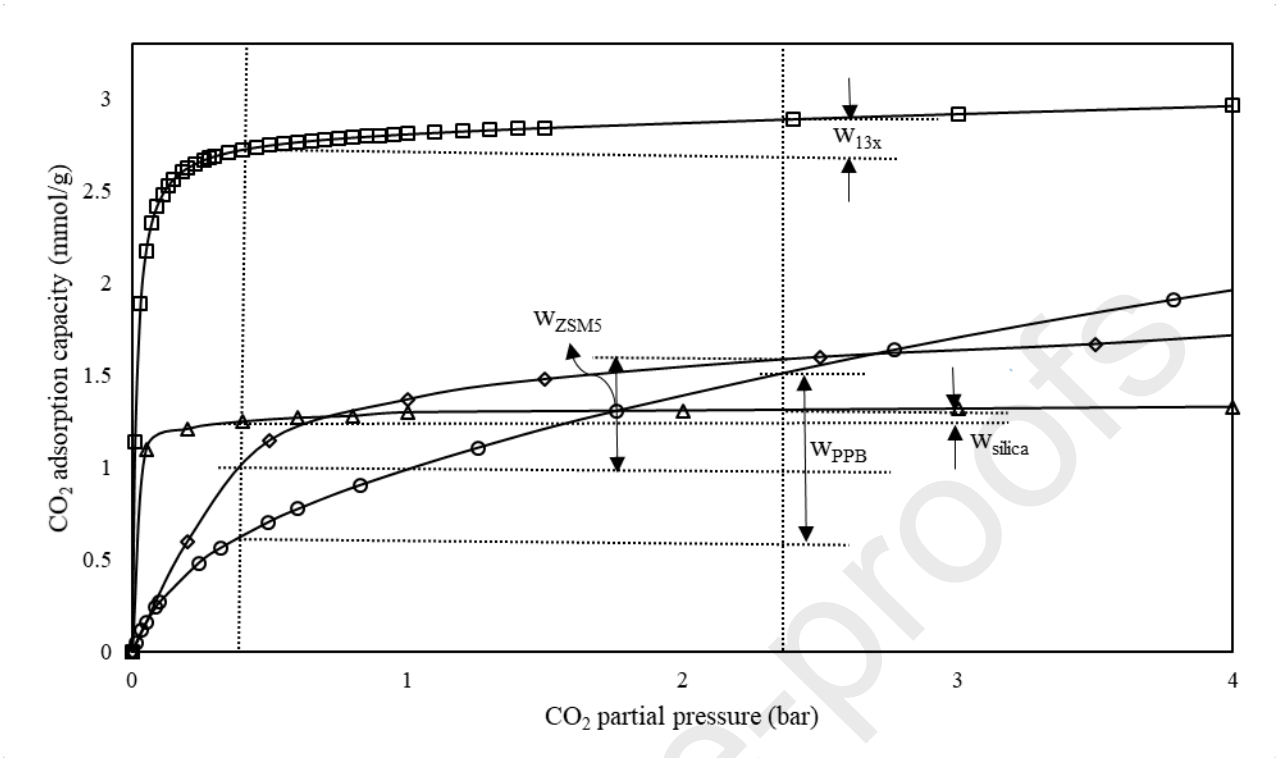

Figure 5: CO_2 adsorption capacity and working capacity (w) of various adsorbents for a 40:60 (vol%) CO_2/CH_4 gas mixture. Legend: (a) ○ PPB adsorbent, (b) □ Zeolite 13x[42], (c) Δ PEI-loaded silica[43], and (d) ◊ ZSM5[44]

5.2 Adsorption breakthrough curves

The measured breakthrough curves of CO_2 and CH_4 at 25 °C and 0 °C are presented in Figure 6. The MTC values in the dynamic PSA simulation model are tuned, so that model outputs fit the experimental breakthrough curves. Therefore, the MTCs for CO_2 and CH_4 at different pressures and temperatures are fitting parameters in the model, and their values are 0.9 1/s and 0.008 1/s, respectively. It was found that temperature and pressure had a negligible effect on the MTCs. It should be noted that the pore size distribution of PPBs was beyond micropore range (> 2 nm), Figure 7a. It is also observed that the measured N_2 isotherm at 77 K (Figure 7b) followed type II

isotherm, according to IUPAC[45], which corresponds to multilayer adsorption on macroporous sorbents.

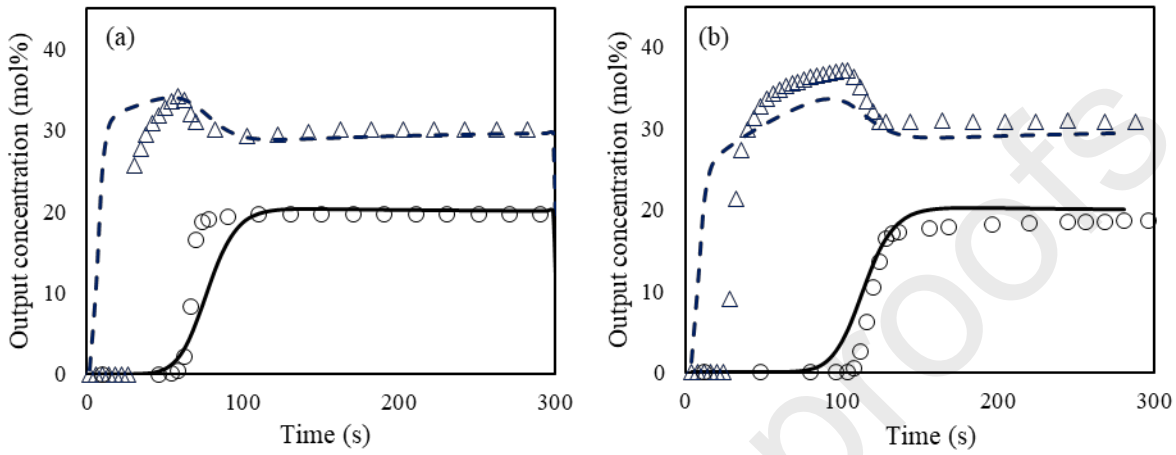

Figure 6: Experimental and breakthrough curves simulated by the model for 2 bar: (a) 25 °C and (b) 0 °C. The simulated biogas compositions and flowrates are tabulated in Table 3. Legend: Δ CH_4 experimental, ○ CO_2 experimental, – – CH_4 modeling, and —— CO_2 modeling.

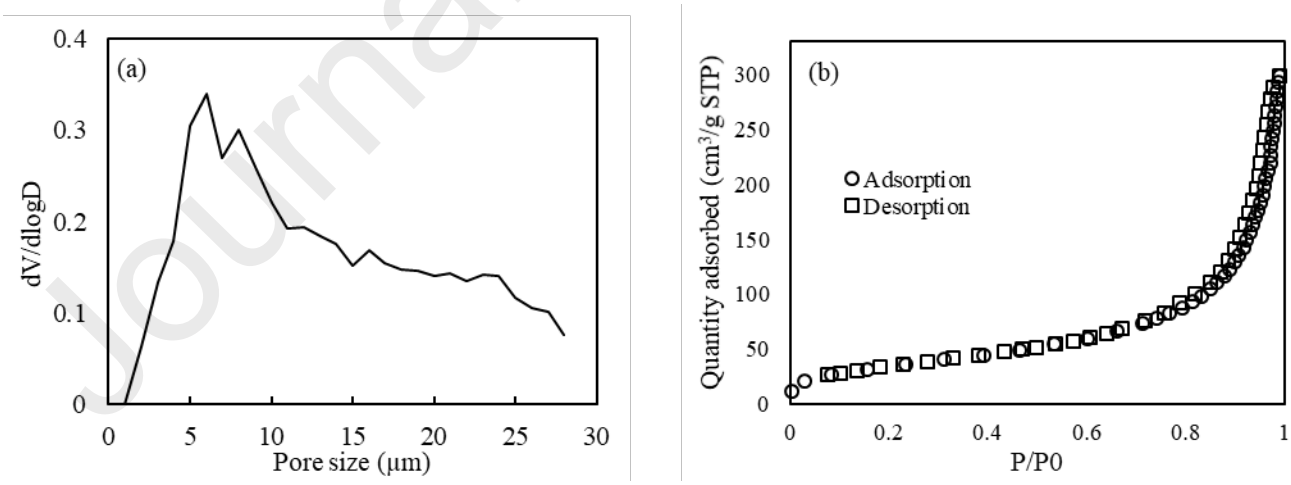

Figure 7: (a) Pore size distribution of PPBs (b) N_2 adsorption desorption isotherm of PPB at 77 K,. Legend: ○ adsorption, □ desorption

Figure 8 presents a sensitivity analysis of MTCs for the breakthrough experiment at 2 bar and 0 °C, and the corresponing fitting correlation coefficients (R^2) are tabulated in Table 5. The optimum MTCs are presented in Case 1 with 0.9 and 0.008 1/s for CO_2 and CH_4, respectively. In Case 2, where the MTC of CH_4 increased to 0.3 1/s, the model could not predict the CH_4 breathrough accurately, and led to a reduction in R^2 of CH_4 from 0.94 to 0.35. In Case 3, MTC of CO_2 was decreased from 0.9 to 0.4 1/s, while the MTC of CH_4 was kept constant at 0.008 1/s. Accordingly, it was seen that the decrease in MTC of CO_2 caused an early breakthrough point and resulted in a reduction in R^2 from 0.95 to 0.81.

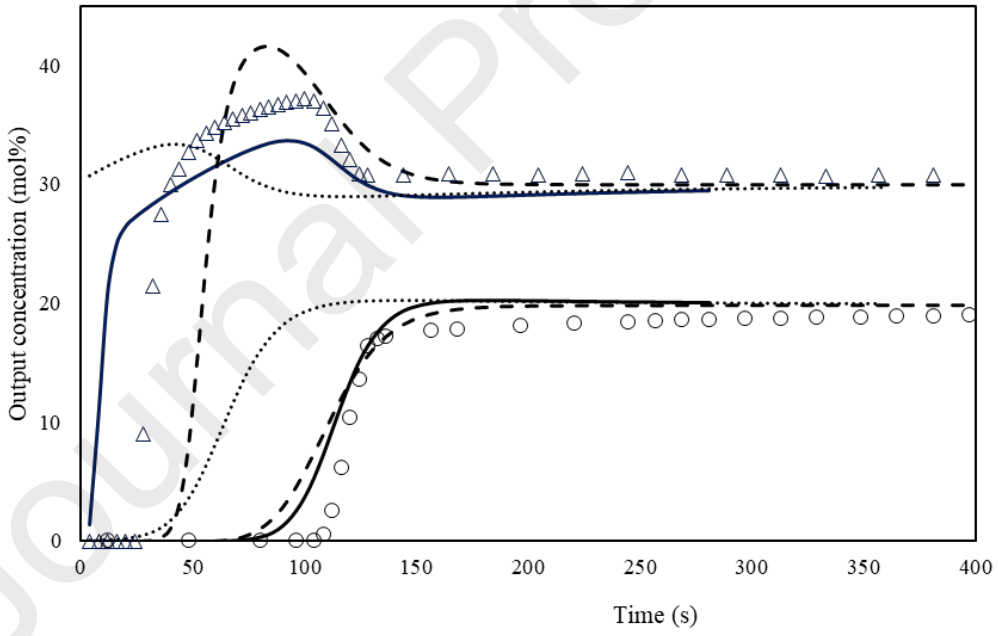

Figure 8: sensitivity analysis of MTCs at 2 bar and 0 °C. Legend: Δ CH_4 experimental, ○ CO_2 experimental, ——— Case 1: MTC (CO_2): 0.9/ MTC (CH_4): 0.008 (1/s), – – – Case 2: MTC (CO_2):0.9 / MTC (CH_4):0.3 (1/s), and ····· Case 3: MTC (CO_2):0.4 / MTC (CH_4):0.008 (1/s)

Table 5: sensitivity analysis of MTCs for breakthrough fitting by model at 2 bar and 0 °C.

	Unit	Case 1	Case 2	Case 3
MTC (CH_4)	(1/s)	0.008	0.3	0.008
MTC (CO_2)	(1/s)	0.9	0.9	0.4
R^2 (CO_2)	(-)	0.95	0.93	0.81
R^2 (CH_4)	(-)	0.94	0.35	0.94

The temperature profile at four different locations along the bed during the breakthrough experiment has been measured (Figure 9). It was observed that the temperature at each location initially rose, due to exothermic gas adsorption process, and then decreased once the adsorbent was saturated, and cooled by exposure to the inlet gas flow. A comparison between experimental and simulated temperature profiles is provided in Figure S1 (Supplementary Information). The temperature profiles of the model and experiment for both 0 ℃ and 25 ℃ show similar trends, reaching the peak values at almost the same time. However, the discrepancy between the simulated and experimental profiles may be due to the slight difference in the breakthrough times[46].

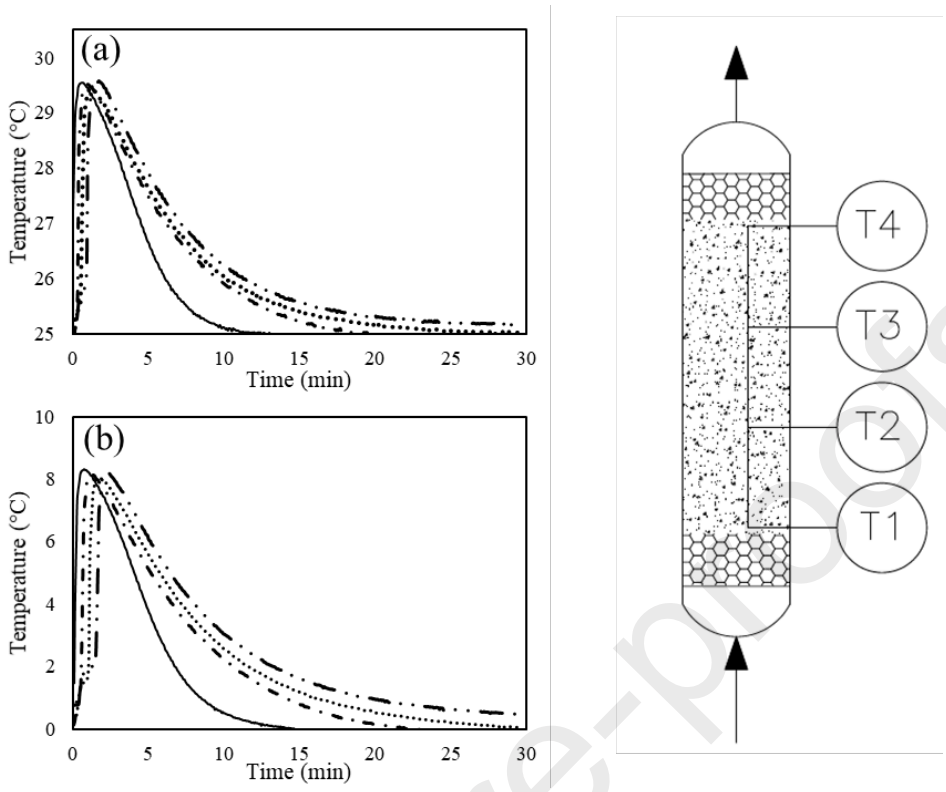

Figure 9: Experimental temperature profile for breakthrough measurement at 2 bar: (a) 25 °C and (b) 0 °C Legend: —— T1, – · – · – T2, ····· T3, and – · · – T4

The dynamic adsorption capacity, CO_2/CH_4 static selectivity and dynamic selectivity based on breakthrough curves have been presented in Figure 10. The initial linear increase in dynamic adsorption capacity correspondences to the breakthrough time (Figure 10a). The CO_2/CH_4 dynamic selectivity (Figure 10b) is much higher than the static selectivity of (Figure 10c), which can be related to the high MTC of CO_2. An increase in temprature led to a reduction in both static and dynamic selectivity, which can be attributed to increased kinetic energy of molecules, and weakening of intermolecular hydrogen bonds[47].

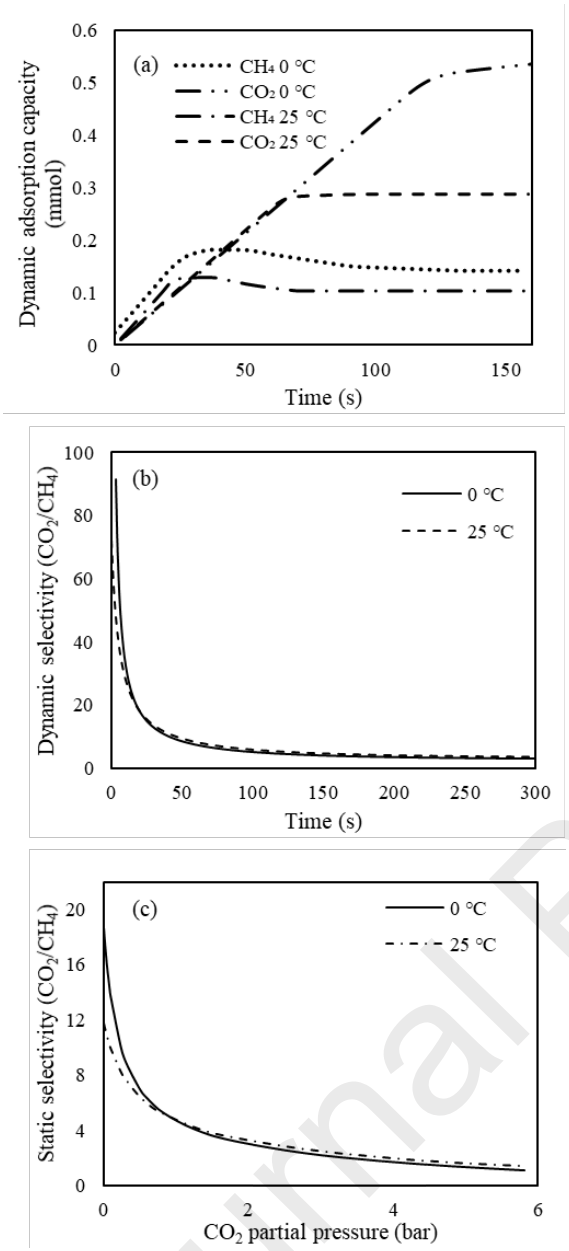

Figure 10: (a) dynamic CO_2 and CH_4 adsorption capacity at 2 bar, and 0 and 25 °C(b) CO_2/CH_4 selectivity dynamic at 2 bar and 0 and 25 °C at bed inlet (c) CO_2/CH_4 static selectivity at 0 and 25 ° C.

5.3 Cyclic adsorption process

The calculated equilibrium parameters using the dual-site Langmuir model along with MTCs were used as inputs to simulate the twin double-bed PSA process presented in Figure 1, with the steps and their durations provided in Figure 2. The MTCs in PSA simulations were assumed to be constant, and measured from breakthrough curves. The feed stream was composed of 40% CO_2 and 60% CH_4. The simulated purity and recovery of biomethane, as well as CO_2 purity in the tail gas for each PSA unit under different scenarios (purge-to-feed ratio (PG/F) and bed length) are presented in Table 6. The minimum biomethane purity at the outlet of the twin double-bed PSA unit should meet the required criteria for injection into the natural gas grid, which varies in the range of 85%-97% for developed countries[48]. Therefore, the objective of this research is to optimise the process to produce biomethane with a minimum purity of 85% and maximum possible recovery, and a tail gas stream with CO_2 concentration suitable for sequestration (>80%)[49–52]. It should be mentioned that although countries like the Netherlands and France require a minimum CH_4 purity of 85%, other countries like Sweden, Spain, and the UK are obligated to a minimum purity of 97%[48].

The combined purity and recovery of the twin double-bed PSA process can be calculated using either Eqs. (14) or (15), and Eq. (17) or (18), respectively. It was seen that there is a ~2% difference between the purity calculated using Eq. (14) and Eq. (15). This discrepancy can be attributed to the fact that although purity and flowrates vary by time, the range of variation in flow rate is much larger (Figure S2 of the Supplementary Information) and can lead to a larger error when averaged values are used. Therefore, Eq. (14) and (17) were selected for further calculation of combined purity and recovery, respectively. The molar flows and composition of feed, internal and product streams of the twin double-bed PSA process were provided in Table

S1 (Supplementary Information). The purge flowrate for a PSA simulation with 5% PG/F value is 5% of feed flow rate (stream F1 of Table S1).

Table 6: Performance of twin double-bed PSA unit for biogas upgrading with high CO_2 purity in tail gas

Run	PG/F		Bed length (mm)		CH_4 purity (%)			CH_4 recovery (%)			CO_2 purity (%)	
	1st	2nd	1st	2nd	1st	2nd	Combined	1st	2nd	Combined	1st	2nd
1	20		13.2		95.8			46.5			51.6	
2	5	5	13.2	10	92.5	92.1	92.4	70.2	69.0	90.8	59.1	75.4
3	5	10	13.2	6	92.5	69	87.1	70.2	70.0	91.1	59.1	80.0

According to Run 1 (Table 6), the produced biomethane in the first PSA unit has a CH_4 purity of 95.8%, but a recovery of 46.5%. Since the recovery in the first PSA unit was low, the PG/F ratio was decreased from 20% to 5% to achieve a higher recovery (Run 2). This resulted in an increase in recovery to 70.2%, but a reduction in purity to 92.5%. To further enhance CH_4 recovery, the twin double-bed PSA process was introduced by adding a secondary PSA to capture the remaining CH_4 in the tail gas of the first PSA unit. Consequently, the overall CH_4 recovery increased to 90.8%. However, the concentration of CO_2 in the tail gas of the second PSA was low (75.4%), and this gas stream could not be stored. Furthermore, it was found that a decrease in the bed length from 10 to 6 cm led to an increase in CO_2 purity in the tail gas of the second PSA unit to 80.0% (Run 3), although the overall CH_4 purity slightly dropped and recovery slightly increased. Although this purity (80:20 (vol%) CO_2/CH_4) is sufficient to meet requirements in some CO_2 sequestrations, the associated energy demand for liquefaction (121

bar at 20 °C) is relatively high. However, upon applying the proposed tail gas sequestration scheme, as illustrated in Figure 11, the average purity of CO_2 in the tail gas increased to 90%, and correspondingly the required pressure for liquefaction at 20 °C was reduced to 78 bar, leading to a reduction in the energy demand for liquefaction. In the proposed scheduling scheme, the tail gas stream is compressed from nearly the end of the BD step until the middle of the PG step, when averaged cumulative CO_2 concentration is 90% (Zone B). The remaining tail gas, produced during BD (Zone A) and the second half of PG (Zone C) steps, with low CO_2 purity, but a significant amount of CH_4 (>20%), can be flared, or alternatively used to generate additional revenue, for example, by CHP. Therefore, this scheduling scheme enables the proposed twin double-bed PSA process to be a NET, rather than a carbon-neutral technology.

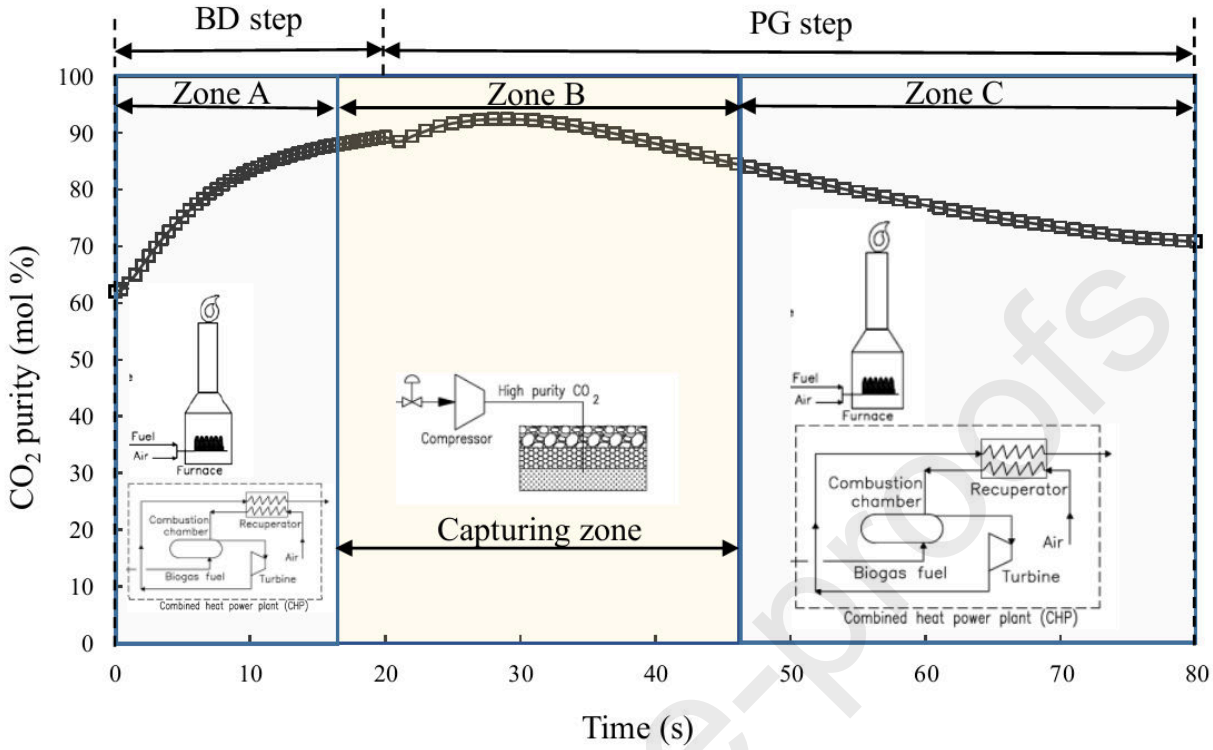

Figure 11: CO_2 purity in the tail gas of the second PSA unit during BD and PG steps: during Zones A and C tail gas is used, and during Zone B highly-concentrated-CO_2 tail gas is stored. Feed pressure and temperature are 6 bar and 25 °C.

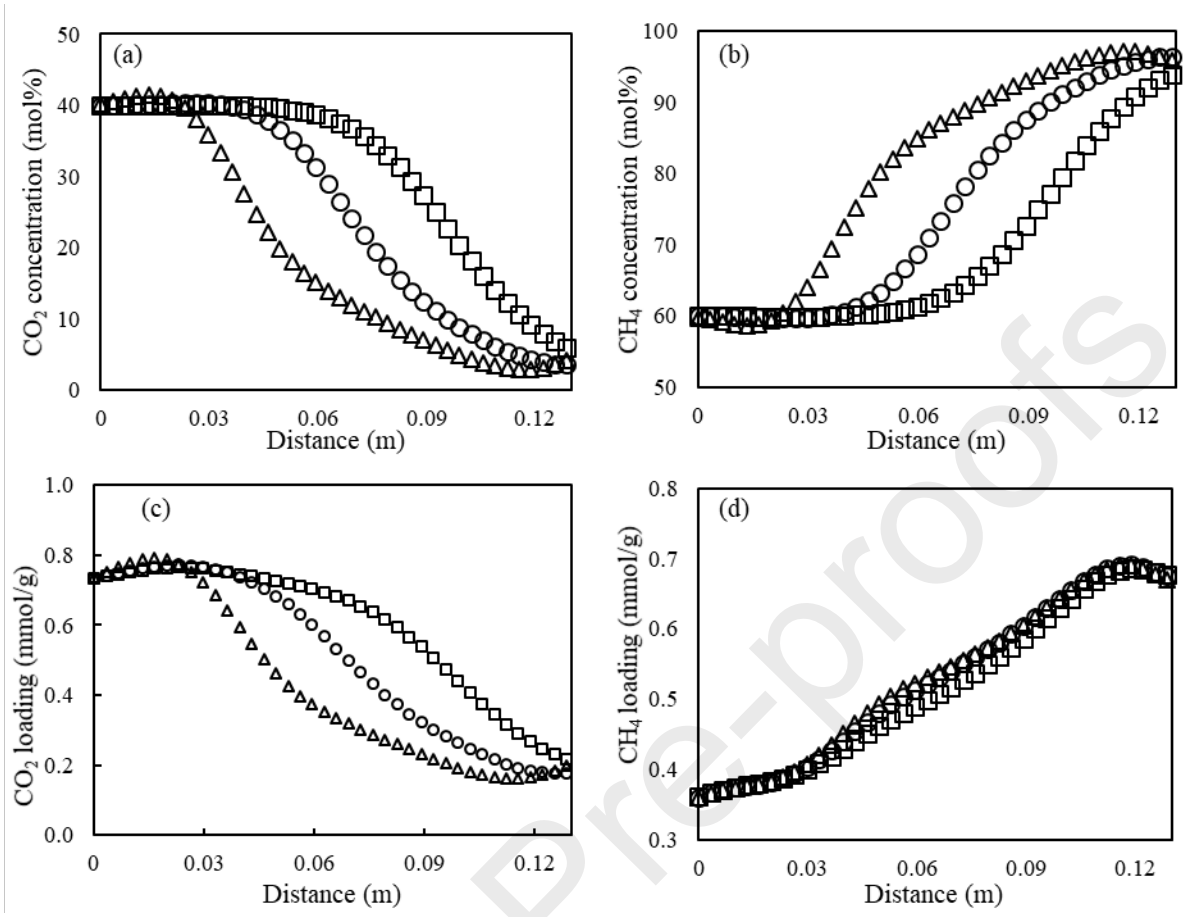

Figure 12: CO_2/CH_4 loading and concentration profiles in the first PSA unit at the beginning (0 s), middle (22 s), and at the end (45 s) of AD step: (a) CO_2 concentration, (b) CH_4 concentration, (c) CO_2 loading, and (d) CH_4 loading. Legend: Δ 0 s (AD start), ○ 22 s (after AD start), and □ 45 s (AD end). Feed pressure and temperature are 6 bar and 25 °C.

To understand the reason for low CH_4 recovery and CO_2 purity in the first PSA unit, their simulated axial concentration and loading profiles during the adsorption step are presented in Figure 12. It can be seen that CO_2 loading is highest near the bed inlet due to high CO_2 concentration. However, by increasing the axial distance, CO_2 concentration decreases, which results in decreasing the CO_2 loading (Figure 12a and c). Moreover, due to the adsorption of

CO_2, CH_4 concentration increases with axial distance (Figure 12b), which results in increased CH_4 loading near the bed outlet (Figure 12d). This rise in CH_4 loading is not favourable since this CH_4 is desorbed during the BD and PG steps, which negatively affects both CH_4 recovery and CO_2 purity. These results show that an important property of adsorbents for biogas upgrading is low CH_4 adsorption capacity to avoid low recovery, but also to increase the purity of CO_2 in the tail gas, especially if CO_2 storage is considered.

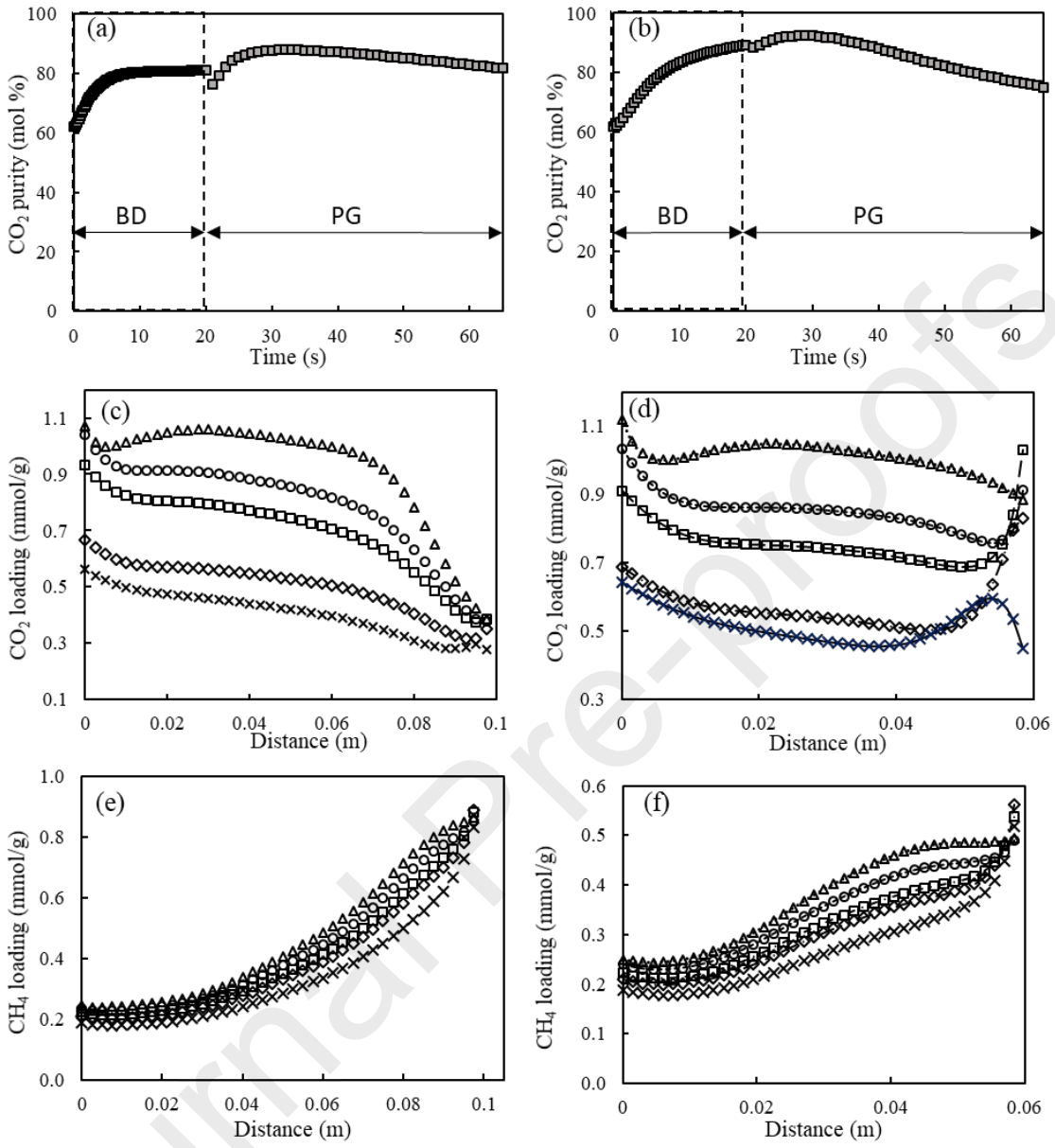

Figure 13: CO_2 purity and CH_4 loading profiles in the second PSA unit: (a/b) CO_2 purity in exit stream during BD and PG, (c/d) CO_2 loading, (e/f) CH_4 loading. L = 10 cm (a/c/e) and L = 6 cm (b/d/f). Legend: Δ 0 s (BD start), ○ 10 s (after BD start), □ 20 s (BD end), ◊ 10 s (after PG start), and × 45 s (PG end). Feed pressure and temperature are 6 bar and 25 °C.

It is noted that a reduction in bed length from 10 cm to 6 cm in the second PSA unit resulted in an increase in CO_2 purity. To further explore this, the transient axial profiles of CH_4 loadings were simulated for bed lengths of 10 cm and 6 cm, and provided (Figure 13). It can be seen that the CO_2 purity continuously increased during the BD step for both bed lengths (Figure 13a and b). This is in agreement with the considerable reduction in CO_2 loading, i.e., a large amount of CO_2 desorbed (Figure 13c and d). On the other hand, during the PG step, the CO_2 purity initially increased (first 10 s), which is then followed by a continuous reduction (Figure 13a and b). The initial increase in CO_2 purity is caused by the sharp decrease in CO_2 loading in the first 10 s of the PG step (Figure 13c and d) that results in desorbing a large amount of CO_2 and reaching the maximum purity. The subsequent reduction in CO_2 purity by the end of PG step is due to the negligible change in CO_2 loading. Moreover, it can be seen (Figure 13e and f) that the CH_4 loading near the end of the longer bed is considerably higher than that of the smaller bed, thus more CH_4 is desorbed during the BD and PG steps, which results in reducing CO_2 purity.

In the proposed twin double-bed PSA configuration, the second PSA unit was introduced as a replacement for the vacuum pump of conventional PVSA. The total energy requirement is 903 kJ/kg CH_4, comprised of 869 kJ/kg CH_4 for the first compressor and 34 kJ/kg CH_4 for the second compressor. In comparison with conventional PVSA units for biomethane production, the proposed configuration benefits from lower required energy demand. For example, the associated energy requirement for PVSA systems developed by Grande et al.[25] , Santos et al.[20] , and Augelletti are 2125, 4500 and 1250 kJ/kg CH_4, respectively. The proposed PVSA system by Wu et al.[26] consumed 944, 2155, and 1093 kJ/kg CH_4electrical energy when MOF, Zeolite 13x,

and CMS-3K were used, respectively. Therefore, the high energy demand of conventional PVSA systems can be attributed to the extreme vacuum requirement for adsorbent regeneration.

6 Conclusions

The current state-of-the-art adsorption units for biogas upgrading are PVSA that require high energy consumption for adsorbent regeneration. To tackle this challenge, in this study PPBs with linear adsorption isotherms and working capacity above atmospheric pressure, as well as acceptable cyclic performance, were developed for CO_2 removal from biogas. The adsorbent was characterised by means of equilibrium isotherms and breakthrough curves obtained from static and dynamic tests, respectively. The dual-site Langmuir model was used to fit the adsorption isotherms, and the MTCs were obtained from fitting the breakthrough curves. The fitting curves and calculated MTCs were used as inputs in a dynamic PSA simulation model to simulate biogas upgrading in a twin double-bed PSA unit without vacuum requirement for adsorbent regeneration. Low CH_4 recovery in the first double-bed PSA unit (70.2%) was improved by the second double-bed PSA, which was used to treat the tail gas of the first unit, resulting in a cumulative CH_4 recovery of 91.1%. In addition to increasing the CH_4 recovery, the second PSA unit increased the average CO_2 purity in the tail gas stream from 59.1% to 80.0%. Although this purity is sufficient to meet requirements in some CO_2 sequestration, a selective tail gas sequestration scheme was proposed, which means compressing CO_2 for storage during the periods when its average purity in the tail gas is above 90%.This approach allows PSA processes, if CO_2 is stored or utilised, to produce carbon-negative rather than carbon-neutral biomethane. Finally, in addition to other adsorbent properties, this study emphasises the benefits

of adsorbents with linear adsorption isotherms and working capacity above atmospheric pressure in order to design PSA processes that do not require energy intensive and costly vacuum.

Acknowledgment

The authors gratefully acknowledge financial support for this work by CoERCe II granted by the Department for Business, Energy and Industrial Strategy (BEIS), UK, BEIS Reference: EEF 5084, and Cambridge Engineering and Analysis Design (CEAD). The authors would like to thank CEAD and 3P INSTRUMENTS GmbH & Co. KG for providing experimental data from which parameters used in the model were derived.

Abbreviations

AA	acrylamide
AD	adsorption
ATM	atmosphere
BD	blow down
BECCS	bioenergy with carbon capture and storage
BPR	back-pressure regulator
CHP	combined heat and power
CSS	cyclic steady state
DSC	differential scanning calorimetry
ED	equalisation de-pressurisation
EP	equalisation pressurisation
EGDMA	ethyleneglycol dimethacrylate
FA	flame arrestor

GA	gas analyser
GHG	greenhouse gas
IPCC	Intergovernmental Panel on Climate Change
MFC	mass flow controller
MOF	metal organic framework
NET	negative-emission technology
ODE	ordinary differential equation
PDE	partial differential equation
PG	purge
PPG	providing purge
PPB	porous polymeric bead
PSA	pressure swing adsorption
PVSA	pressure vacuum swing adsorption
RP	re-pressurisation
TSA	temperature swing adsorption

Nomenclature

Item	Description	Unit
a	surface area	m^2/m^3
A	area	m^2
c	concentration	mol/m^3
C	molar specific heat capacity	J/(mol·K)
D	diffusivity coefficient	m^2/s
D_z	axial dispersion coefficient	m^2/s
d	diameter	m

h	heat transfer coefficient	W/(m^2·s)
k	thermal conductivity	W/(m·K)
M	molecular weight	g/mol
m	adsorbent mass	kg
MTC	mass transfer coefficient (LDF model)	1/s
Nu	Nusselt number	(-)
P	pressure	bar
Pr	Prandtl number	(-)
q	loading	mol/kg
Q_t	Feed volumetric flowrate	m^3/s
Ra	Rayleigh number	(-)
Re	Reynolds number	(-)
r	radius	m
T	temperature	K
t	time	s
u	velocity	m/s
W	working capacity	mol/kg
y	mole fraction in gas phase	(-)
ΔH	heat of adsorption	J/mol

Greek letters

ϵ	porosity	(-)
μ	viscosity	kg/(m·s)
ρ	density	kg/m^3
τ	tortuosity factor	(-)

λ	thermal conductivity	J/(s·m·K)

Subscripts

ads	adsorbate or adsorption
atm	atmosphere
a	air
b	bed
f	film or feed (end)
g	gas phase
i	component *i* or inside
o	outside
p	particle or product end
PG	purge
RP	re-pressurisation
s	superficial
T	total
t	tail gas
v	constant volume
w	wall

References

1 R. J. Millar, J. S. Fuglestvedt, P. Friedlingstein, J. Rogelj, M. J. Grubb, H. D. Matthews, R. B. Skeie, P. M. Forster, D. J. Frame and M. R. Allen, *Nat. Geosci.*, 2017, **10**, 741–747.

2 M. Fajardy, S. Chiquier and N. Mac Dowell, *Energy Environ. Sci.*, 2018, **11**, 3408–3430.

3 E. Kriegler, N. Bauer, A. Popp, F. Humpenöder, M. Leimbach, J. Strefler, L. Baumstark, B. L. Bodirsky, J.

Hilaire and D. Klein, *Glob. Environ. Chang.*, 2017, **42**, 297–315.

4 A. S. Brouwer, M. van den Broek, W. Zappa, W. C. Turkenburg and A. Faaij, *Appl. Energy*, 2016, **161**, 48–74.

5 J. Bacenetti, A. Fusi and A. Azapagic, *Sci. Total Environ.*, 2019, **658**, 684–696.

6 Y. Yang, C. Y. Chuah, L. Nie and T. H. Bae, *J. Memb. Sci.*, 2019, **569**, 149–156.

7 J. Bacenetti, A. Fusi and A. Azapagic, *Sci. Total Environ.*, 2019, **658**, 684–696.

8 E. Esposito, L. Dellamuzia, U. Moretti, A. Fuoco, L. Giorno and J. C. Jansen, *Energy Environ. Sci.*, 2019, **12**, 281–289.

9 R. Baciocchi, E. Carnevale, A. Corti, G. Costa, L. Lombardi, T. Olivieri, L. Zanchi and D. Zingaretti, *Biomass and Bioenergy*, 2013, **53**, 128–137.

10 J. Koornneef, P. van Breevoort, P. Noothout, C. Hendriks and L. Luning, 2013, 1–101.

11 L. Lombardi and E. Carnevale, *Energy*, 2013, **62**, 88–94.

12 R. L. S. Canevesi, K. A. Andreassen, E. A. Da Silva, C. E. Borba and C. A. Grande, *Ind. Eng. Chem. Res.*, 2018, **57**, 8057–8067.

13 K. Arrhenius, A. Fischer and O. Büker, *Appl. Sci.*, 2019, **9**, 1171.

14 A. C. Elwell, N. H. Elsayed, J. N. Kuhn and B. Joseph, *Waste Manag.*, 2018, **73**, 189–196.

15 A. Golmakani, S. Fatemi and J. Tamnanloo, *Sep. Purif. Technol.*, , DOI:10.1016/j.seppur.2016.11.030.

16 H. Vogtenhuber, R. Hofmann, F. Helminger and G. Schöny, *Energy*, 2018, **162**, 200–209.

17 I. Angelidaki, L. Treu, P. Tsapekos, G. Luo, S. Campanaro, H. Wenzel and P. G. Kougias, *Biotechnol. Adv.*, 2018, **36**, 452–466.

18 P. Rzepka, A. B. Jasso-Salcedo, A. Janicevs, P. Vasiliev and N. Hedin, *Energy Procedia*, 2019, **158**, 6715–6722.

19 P. Sutradhar, P. Maity, S. Kar and S. Poddar, *Int. J. Innov. Technol. Explor. Eng.*, 2019, **8**, 64–69.

20 M. P. S. Santos, C. A. Grande and A. E. Rodrigues, *Ind. Eng. Chem. Res.*, 2011, **50**, 974–985.

21 R. Augelletti, M. Conti and M. C. Annesini, *J. Clean. Prod.*, 2017, **140**, 1390–1398.

22 L. Mafra, T. Čendak, S. Schneider, P. V. Wiper, J. Pires, J. R. B. Gomes and M. L. Pinto, *Chem. Eng. J.*, 2018, **336**, 612–621.

23 S. Sutanto, J. W. Dijkstra, J. A. Z. Pieterse, J. Boon, P. Hauwert and D. W. F. Brilman, *Sep. Purif. Technol.*, 2017, **184**, 12–25.

24 Y. Meng, J. Jiang, Y. Gao, A. Aihemaiti, T. Ju, Y. Xu and N. Liu, *Chem. Eng. J.*, 2019, **361**, 294–303.

25 C. A. Grande and A. E. Rodrigues, *Ind. Eng. Chem. Res.*, 2007, **46**, 7844–7848.

26 B. Wu, X. Zhang, Y. Xu, D. Bao and S. Zhang, *J. Clean. Prod.*, 2015, **101**, 251–261.

27 N. Wakao and T. Funazkri, *Chem. Eng. Sci.*, 1978, **33**, 1375–1384.

28 R. T. Yang, *Gas separation by adsorption processes*, Butterworth-Heinemann, 2013.

29 N. Wakao, S. Kaguei and T. Funazkri, *Chem. Eng. Sci.*, 1979, **34**, 325–336.

30 R. C. Reid, J. M. Prausnitz and B. E. Poling, .

31 R. B. Bird, *Appl. Mech. Rev.*, 2002, **55**, R1–R4.

32 T. L. P. Dantas, F. M. T. Luna, I. J. Silva Jr, D. C. S. de Azevedo, C. A. Grande, A. E. Rodrigues and R. F. P. M. Moreira, *Chem. Eng. J.*, 2011, **169**, 11–19.

33 T. L. P. Dantas, S. M. Amorim, F. M. T. Luna, I. J. Silva, D. C. S. de Azevedo, A. E. Rodrigues and R. F. P. M. Moreira, *Sep. Sci. Technol.*, 2009, **45**, 73–84.

34 G. C. Vliet, .

35 S. W. Churchill and H. H. S. Chu, *Int. J. Heat Mass Transf.*, 1975, **18**, 1049–1053.

36 J. Yang and C. Lee, *AIChE J.*, 1998, **44**, 1325–1334.

37 C. Sereno and A. Rodrigues, *Gas Sep. Purif.*, 1993, **7**, 167–174.

38 A. P. T. Code, *Am. Soc. Mech. Eng. New York*.

39 T. M. McDonald, W. R. Lee, J. A. Mason, B. M. Wiers, C. S. Hong and J. R. Long, *J. Am. Chem. Soc.*, 2012, **134**, 7056–7065.

40 S. Xian, Y. Wu, J. Wu, X. Wang and J. Xiao, *Ind. Eng. Chem. Res.*, 2015, **54**, 11151–11158.

41 R. Serna-Guerrero and A. Sayari, *Chem. Eng. J.*, 2010, **161**, 182–190.

42 P. Xiao, J. Zhang, P. Webley, G. Li, R. Singh and R. Todd, *Adsorption*, 2008, **14**, 575–582.

43 R. Kishor and A. K. Ghoshal, *Chem. Eng. J.*, 2016, **300**, 236–244.

44 J. Tamnanloo, S. Fatemi and A. Golmakani, *Adsorpt. Sci. Technol.*, 2014, **32**, 707–716.

45 K. S. W. Sing, *Pure Appl. Chem.*, 1985, **57**, 603–619.

46 N. S. Wilkins and A. Rajendran, *Adsorption*, 2019, **25**, 115–133.

47 S. A. Nabavi, G. T. Vladisavljević, Y. Zhu and V. Manović, *Environ. Sci. Technol.*, 2017, **51**, 11476–11483.

48 O. W. Awe, Y. Zhao, A. Nzihou, D. P. Minh and N. Lyczko, *Waste and Biomass Valorization*, 2017, **8**, 267–283.

49 A. Hortle, P. de Caritat, C. Stalvies and C. Jenkins, *Energy Procedia*, 2011, **4**, 5495–5503.

50 S. Sharma, P. Cook, C. Jenkins, T. Steeper, M. Lees and N. Ranasinghe, *Energy Procedia*, 2011, **4**, 5447–5454.

51 T. Pieri, A. Nikitas, A. Castillo-Castillo and A. Angelis-Dimakis, *Environments*, 2018, **5**, 108.

52 P. Girdon, P.; Gloger, C.; Gonzalez, D.; Henneqiun, J.; Krinninger, K.; de Lorenzi, L.; Wilyman, *Minimum Specifications for Food Gas Applications*, Brussels, Belgium, 2006.

Supplementary Information

Table S1: Molar flows and composition of feed, internal and product streams of the double PSA process

Stream	Description	Duration	Flow rate		Composition (vol%)	
		s	SCCM	kmol/s $\times 10^{-07}$	CO_2	CH_4
F1 AD	Feed to 1st PSA at AD step	45	792	5.89	40	60
F1 RP	Feed to 1st PSA at RP step	20	754	5.61	40	60
F2	Effluent product from 1st PSA at AD step	45	515	3.82	7.5	92.5
F3	Feed to 2nd PSA at AD and RP steps	65	434	3.23	59.1	40.9
F4	Effluent product from 2nd PSA at AD step	45	241	1.79	31	69
F5	Effluent tail gas from 2nd PSA during BD & PG steps	65	215	1.59	78.1	21.9

Flow rates are at standard conditions: 0 °C and 1 atm, the streams refer to Figure 1

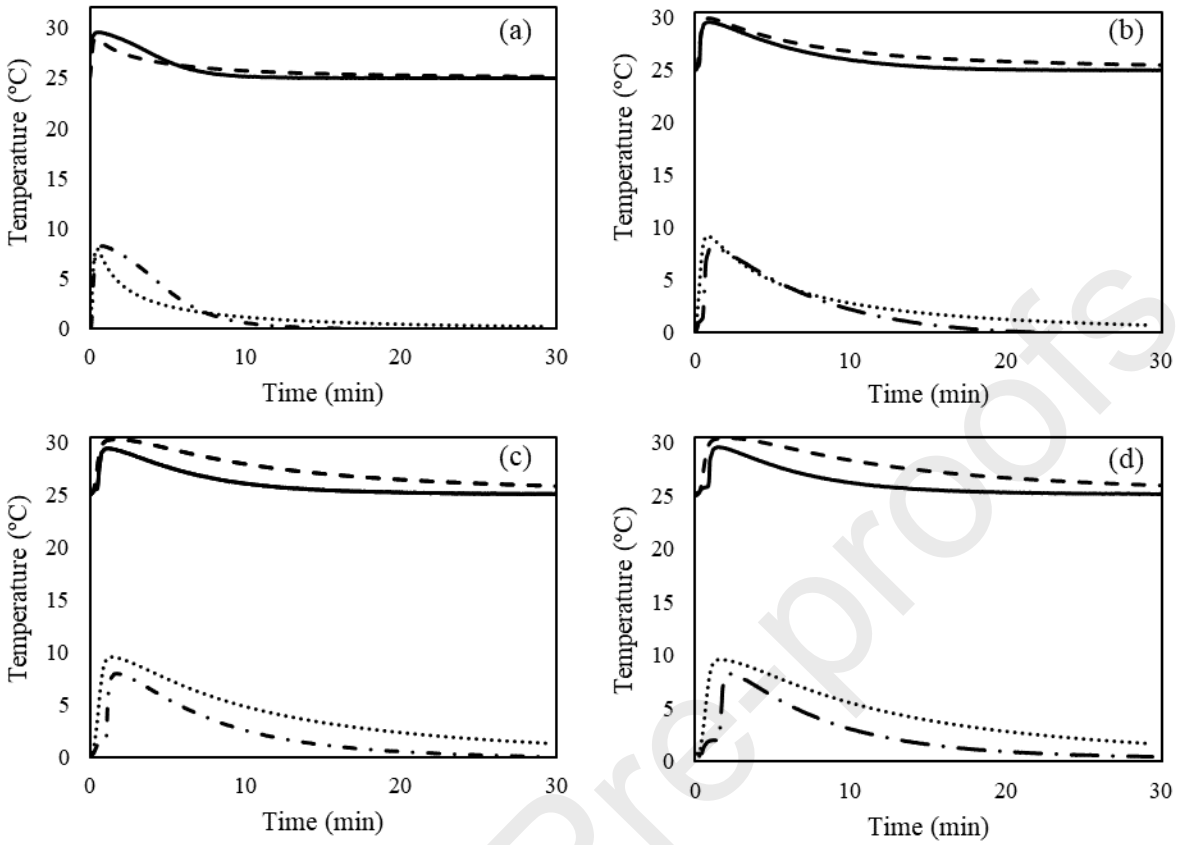

Figure S1: Experimental and simulated temperature profile for breakthrough measurements at 2 bar, Legend: —— 25 °C Experiment, – – – 25 °C Model, – · – · – 0 °C Experiment, and 0 °C Model ·····

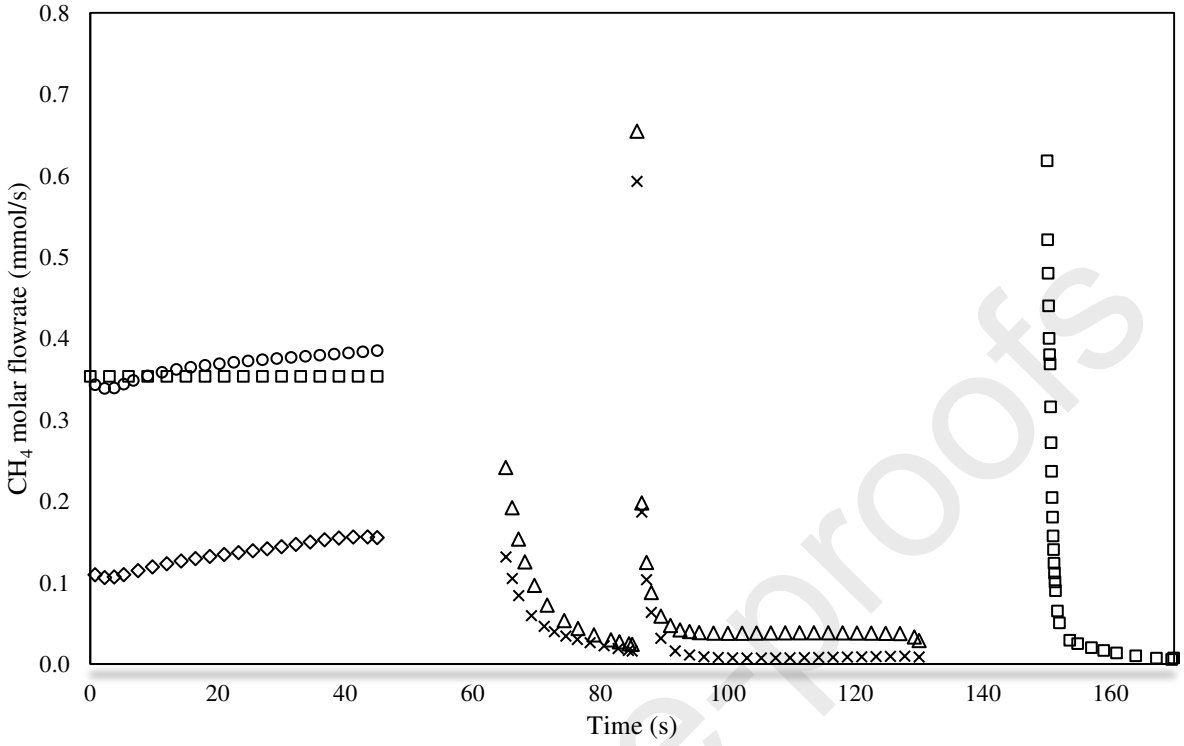

Figure S2: CH_4 molar flowrate after reaching CSS condition. Legend: □ F1 molar flowrate of CH_4 to 1st PSA, ○ F2 effluent product CH_4 molar flowrate from 1st PSA, Δ F3 CH_4 feed molar flowrate to 2nd PSA, ◊ F4 CH_4 effluent product molar flowrate from 2nd PSA, and × F5 effluent tail gas CH_4 molar flowrate from 2nd PSA

Declaration of Competing Interest

The authors declare that they have no known competing financial interests or personal relationships that could have appeared to influence the work reported in this paper.

Highlights:

Carbon dioxide is removed and biogas upgraded to biomethane

A twin double-bed pressure swing adsorption process is proposed for biogas upgrading

Novel porous polymeric beads are employed as adsorbents for carbon dioxide

Selective tail gas sequestration is a carbon-negative route for biomethane production